Experimental Correlation of Mechanical Properties of the Ti-6Al-4V Alloy at Different Length Scales

Víctor Tuninetti [1,*], Andrés Felipe Jaramillo [1], Guiomar Riu [2], Carlos Rojas-Ulloa [1], Amna Znaidi [3], Carlos Medina [4], Antonio Manuel Mateo [2] and Joan Josep Roa [2,*]

[1] Department of Mechanical Engineering, Universidad de La Frontera, 4780000 Temuco, Chile; andresfelipe.jaramillo@ufrontera.cl (A.F.J.); c.rojas13@ufromail.cl (C.R.-U.)
[2] Department of Materials Science and Engineering (CIEFMA), Barcelona School of Engineering (EEBE), Universitat Politècnica de Catalunya-BarcelonaTech, 08019 Barcelona, Spain; guiomarriu@gmail.com (G.R.); antonio.manuel.mateo@upc.edu (A.M.M.)
[3] Laboratory of Applied Mechanics and Engineering LR-MAI, University Tunis El Manar–ENIT BP37, Tunis 1068, Tunisia; amna.znaidi@ipeiem.utm.tn
[4] Department of Mechanical Engineering, Universidad de Concepción, 4030000 Concepción, Chile; cmedinam@udec.cl
* Correspondence: victor.tuninetti@ufrontera.cl (V.T.); joan.josep.roa@upc.edu (J.J.R.); Tel.: +56-452325984 (V.T.); +34-93-413-41-39 (J.J.R.)

Abstract: This article focuses on a systematic study of a Ti-6Al-4V alloy in order to extensively characterize the main mechanical properties at the macro-, micro- and submicrometric length scale under different stress fields. Hardness, elastic modulus, true stress–strain curves and strain-hardening exponent are correlated with the intrinsic properties of the α- and β-phases that constitute this alloy. A systematic characterization process followed, considering the anisotropic effect on both orthogonal crystallographic directions, as well as determining the intrinsic properties for the α-phase. An analytical relationship was established between the flow stress determined under different stress fields, testing geometries and length scales, highlighting that it is possible to estimate flow stress under compression and/or tensile loading from the composite hardness value obtained by instrumented nanoindentation testing.

Keywords: titanium alloys; plastic anisotropy; tension–compression asymmetry; mechanical properties; nanohardness; Young's modulus; tensile–compression tests

1. Introduction

Titanium alloys are attractive engineering materials for the aerospace industry, mainly because of their high specific strength and ductility at low and moderate temperatures [1–3]. In particular, Ti-6Al-4V is the most widely used titanium alloy due to a proper balance of processing characteristics such as good castability, plastic workability, heat treatability and weldability [4]. In recent years, the deformation processes operating in α- and β-phase titanium alloys have been extensively investigated by means of advanced characterization techniques [5–7]. The predominant constituent phase of this Ti-alloy, low-symmetry hexagonal-structured α-phase, as well as α-/β-interfaces, exhibit remarkable elastic and plastic anisotropy [8,9]. The primary cause of the anisotropic behavior of polycrystalline alloys is the preferred orientation of grains, crystallographic textures, due to working processes [10]. Therefore, properties of polycrystals can be computed as averages of weighted values from the individual crystal orientations based on the texture [11].

The Ti-6Al-4V alloy is well known to exhibit anisotropic mechanical behavior throughout the elastoplastic range, as reported in [2,8,12–14]. This anisotropic behavior is commonly characterized by properties such as Young's modulus, initial flow stress and strain-hardening rate obtained from tensile and compression tests in different directions of the material [10,15–17]. In recent years, the nanoindentation technique has been presented as

an alternative to the conventional testing methods because it is simple, fast, nondestructive, relatively inexpensive and requires a minimum amount of material [18–20].

In this context, the stress and strain states induced by instrumented nanoindentation are clearly different from the states in uniaxial testing. The deformation field induced by a sharp nanoindenter also varies according to the analyzed location. Biaxial stretched regions are localized in the surface surrounding the indentation imprint, and the region directly below the nanoindenter tip exhibits compressive triaxial deformations. It is worth noting that the stretched area appears because much of the portion of the material presents an elastic strain field, and the plastic region is localized very close to the indenter tip. The elastic zone acts as a rigid body imposing displacement constraints to the plastic zone, producing a triaxial or combined stress state. As is clearly evident in the literature, the investigation of mechanical behavior at the local length scale constitutes a fundamental and active research topic for Ti-6Al-4V alloys, as found in [21–23]. It is well established that the mechanical response at the micrometric and submicrometric length scales differs fundamentally from the bulk material response determined by means of conventional tensile and compression tests. Uchic and Dimiduk [24] demonstrated that yield strength increases by decreasing the length scale. Furthermore, as described by Broitman [25], hardness obtained by this nanoindentation method is closely related to the plastic deformation of the surface and other mechanical properties of materials such as creep strength, ductility and fatigue resistance.

In the present work, the nanoindentation technique was used with the aim of identifying the anisotropic behavior of the Ti-6Al-4V alloy and establishing a relationship between its macroscopic and micro-/submicrometric mechanical properties. Systematic sets of tensile, compression and nanoindentation tests, performed in two orthogonal material directions, were obtained to correlate the different length scales behavior. In addition, advanced characterization techniques, such as field-emission scanning electron microscopy, were used to investigate the plastic deformation induced at the nanometric length scale under complex stress fields.

2. Materials and Methods

2.1. Sample Preparation

The material analyzed in this research was a two-phase near-alpha Ti-6Al-4V alloy. The sample had a prismatic geometry, with dimensions of 60 mm × 140 mm × 40 mm (Figure 1). Mean grain size was measured following the linear intercept method on micrographs taken with a field-emission scanning electron microscope (FESEM), resulting in equivalent ellipsoidal grain size with a length and width of 12 ± 3 and 6 ± 2 µm, respectively. The chemical composition directly determined by energy-dispersive X-ray spectroscopy (EDS) is summarized in Table 1. Before nanoindentation tests, the surface of the specimens was ground and polished using silicon carbide abrasive papers, subsequently with a diamond suspension of decreasing particle size (30, 6, 3 and 1 µm), and finalizing with a colloidal alumina suspension polishing step.

2.2. Mechanical Properties at the Macro- and Nanoscales

2.2.1. Macroscale: Tensile and Compression Tests

The tensile specimens were machined following the EN 10002-1 standard, and the compression specimens were obtained following the instructions presented in [26] (see Figure 2). Anisotropic effect was investigated with specimens machined from the two orthogonal directions (longitudinal direction (LD) and transversal direction (TD)) for both loading conditions.
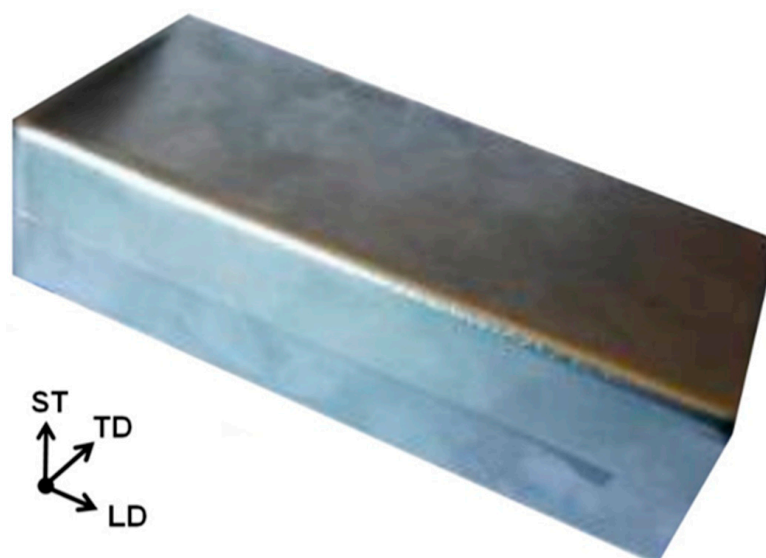
Figure 1. Ti-6Al-4V alloy ingot, where ST, TD and LD correspond to short transverse, transversal and longitudinal directions, respectively.

Table 1. Chemical composition of the studied Ti-6Al-4V alloy (wt.%).

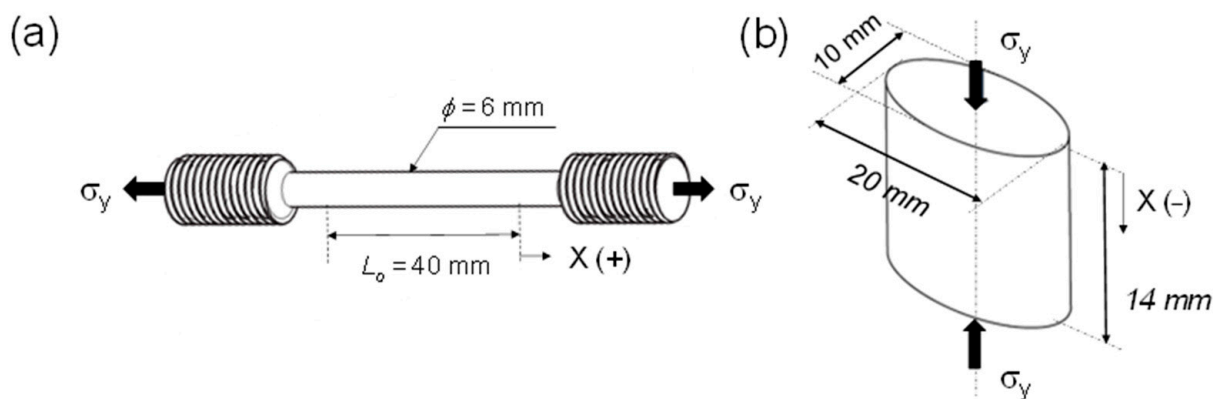| Al	V	Fe	N	O	C	Ti
6.1	4.0	0.3	0.05	0.2	0.08	Bal.

Figure 2. Schematic representation of the different specimens used in the macroscopic tests. (**a**) Tensile and (**b**) compression specimens. σ_y and X denote the direction of the stress and the displacement associated with the tensile and compressive loadings. The positive and negative signs of the displacements correspond to the lengthening and shortening of the gauge length, respectively.

Quasistatic uniaxial tensile tests were performed with a constant true elastoplastic strain rate of 1×10^{-3} s^{-1} at room temperature, following the methodology proposed in [27]. A Zwick uniaxial electromechanical testing machine equipped with a MultiSens light extensometer was used. As is well known, some mechanical properties are sensitive to the strain rate employed to conduct the tests. In this sense, the difference in strain rates between the performed macroscopic and nanoindentation tests leads to negligible variations in the computation of the mechanical properties. According to previous tests performed in these specimens [2,17], the average indentation strain rate of 0.05 s^{-1} produces a yield strength and elastic modulus slightly higher than those reported by around 2%. This error could be avoided by selecting a strain rate equal to 10^{-3} s^{-1} for the nanoindentation tests. However, this is not straightforward since an accurate material model is required due to the

lack of homogeneity caused by the induced triaxial strains in the deformed material. Compression tests were performed with a servohydraulic testing machine (Schenck Hydropuls), and an optical system allowed determining the evolving loading area to compute more accurate stress [28]. Both types of experiments were performed under the displacement control mode. A minimum of three samples were tested per condition and direction in order to reveal standard deviations of mechanical properties.

The uniaxial true tensile strain was measured using an extensometer until a strain level of 0.1 was reached. Furthermore, the optical measurement system was coupled in the experimental set-up in order to compute the hardening rate until a true strain of 0.43 was reached.

2.2.2. Nanoscale: Nanoindentation Tests

Mechanical characterization of the Ti-6Al-4V alloy included the evaluation of its effective hardness (H) and elastic modulus (E) through the instrumented indentation technique. Nanoindentation tests were performed on a nanoindenter XP (MTS) for experiments performed at 2000 nm of maximum displacement into the surface, and the experiments 700 nm were performed with iNano equipment (Nanomechanics, Inc., Oak Ridge, TN, USA). Both nanoindenters are equipped with a continuous stiffness measurement module, allowing a dynamic determination of the mechanical properties, such as hardness and elastic modulus, during the indentation process. A Berkovich tip was used, and experimental data were analyzed using the Oliver and Pharr method [29,30]. Calibration of the contact area of the tip was performed with fused silica (known value of Young's modulus of 72 GPa and Poisson's ratio of 0.17 [29]). Along the indentation process, the indentation strain rate was held at 0.05 s^{-1}.

Two different sets of experiments, at the micro- and nanometric length scale, were performed under the displacement loading mode. The mechanical response of the polycrystalline alloy was assessed as the average behavior of 25 imprints (5×5), performed at 2000 nm of the maximum displacement into the surface or until reaching the maximum applied load of 650 mN. A constant distance of 25 µm between imprints was held in order to avoid any overlapping effect. On the other hand, to evaluate the intrinsic mechanical properties for the α-phase, homogeneous indentation arrays of 16 imprints (4×4) were performed in five different zones at 700 nm of maximum displacement into the surface, which implies a maximum applied load of around 50 mN. Again, a distance of about 25 µm was kept from other indentations.

2.3. Surface Assessment

Deformation evolution induced during the nanoindentation process was observed using two devices: a focused ion beam (FIB) using a dual beam (FIB)/field-emission scanning electron microscope (Carl Zeiss Neon 40, Oberkochen, Germany) operating at 20 kV for residual imprints at 2000 nm, and a scanning electron microscope Su 3500 (Hitachi, Tokyo, Japan) for 700 nm imprints.

3. Results and Discussion

3.1. Microstructure

The microstructure of the studied Ti-6Al-4V alloy consists of primary, hexagonal, closely packed (hcp) α-grains embedded in a bi-phased matrix, as depicted in Figure 3. The matrix is composed of alternating lamellae of a primary α-phase and body-centered cubic (bcc) β-phase. Here, the α-phase appears in gray, and the β-phase appears in white. The phases' proportions were quantified using five different FESEM micrographs randomly recorded, with the α-phase found in 94% of the area and the β-phase in the rest.
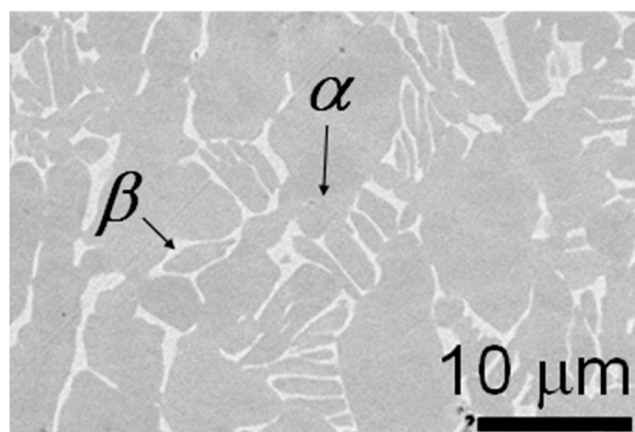
Figure 3. FESEM micrograph view of the Ti-6Al-4V alloy showing the heterogeneous distribution of the α-/β-phases.

3.2. Tensile and Compression Properties

The true stress (σ)–true strain (ε) curves for all the studied conditions are presented in Figure 4a, and the postprocessed data are summarized in Table 2. It is necessary to mention that the Young's modulus was determined from the elastic part of the σ–ε curve in the range of 50–95% of the elastic limit. From the summarized data, it can be seen that the yield strength and the total elongation for the specimens under study are strongly dependent on the loading stress induced in the specimen, with the values reported being higher when the specimen is deformed under compression. Furthermore, these curves reveal that the yield strength determined, though the compressive loading is slightly higher than those determined under tensile loading stress, around 4.42 and 11.5% for the LD and TD directions, respectively. According to the observed behavior, the alloy studied presents an anisotropic yielding and anisotropic hardening effect, with a higher yield in the TD direction than the LD direction. Furthermore, as shown in Figure 4a, during uniaxial loading, the initial hardening rate is always higher in compression than in tension, as reported in [31–33]. On the other hand, from the strain-hardening rate, as a function of the flow stress (Figure 4b), the related deformation process induced under different loading stresses can be extracted, primarily in terms of dislocations. Here, only two stages (I and II) appear. Stage I is based on dipole trapping, which results from edge dislocations of a single Burgers vector of opposite signs, inducing a gliding process on parallel planes and, and a result, inducing an attractive force [34]. Stage II is most easily understood in terms of a real glide, whereby dislocation loops expand across the slip plane and deposit loops around local hard spots [35].
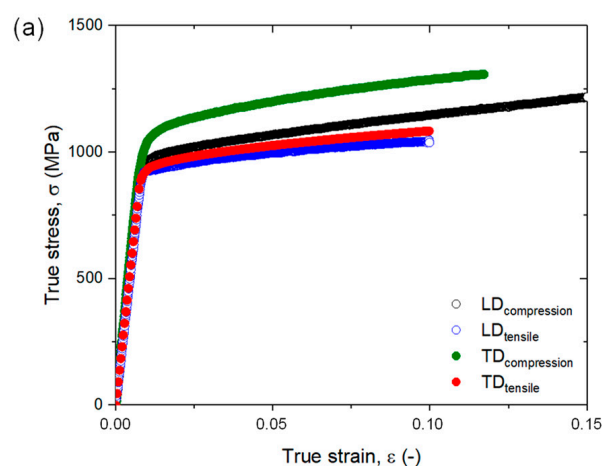

Figure 4. *Cont.*
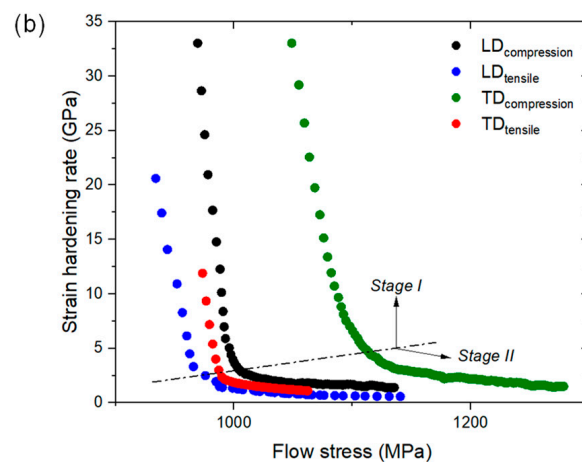
Figure 4. (**a**) True stress vs. true strain representation and (**b**) strain-hardening rate vs. flow stress for the tensile and compression tests performed in two different orthogonal directions (LD and TD).

As shown in Table 2, the elastic-to-plastic transition determined from the tensile and compressive stress–strain curves of the investigated Ti-6Al-4V alloy (Figure 4a) exhibits significant differences in the initial yielding stress value. However, as shown in Figure 4b, the strain-hardening rate exhibits a similar behavior within Stages I and II. This representation highlights the yielding asymmetry effect between tension and compression, generally known as the strength differential effect (SDE), a phenomenon mainly characterized at different strains or plastic work levels. The mechanical properties summarized in Table 2 show a strong anisotropic effect, as reported in previous works [10,12,15,17].

The strain-hardening behavior of metals is mainly dictated by the ability of defects to rearrange into energy-minimizing structures, as widely investigated [36]. The most commonly used strength models were developed to capture strain-hardening behavior due to the reorganization of dislocation networks. Some models employ a parabolic [37,38] or exponential function [39] to capture the transition from linear hardening to dynamic recovery [38], which can be physically connected to the evolution of dislocation populations [40–44]. Within this context, and from the experimental values of stress–strain under tension and compression, the strain-hardening exponent (n) is determined considering the well-known Hollomon power law relationship [45]. Figure 5 shows a log-log representation of true stress and true plastic strain, showing the presence of two different n exponents at a similar plastic strain threshold of 1.83% for all the investigated specimens. The two different distinguished regions are as follows:

Region 1: from $0 \leq \varepsilon_p$ (%) ≤ 1.83 (denoted as n_{R1});
Region 2: from $1.83 \leq \varepsilon_p$ (%) ≤ 9 (denoted as n_{R2}).

The strain-hardening exponent as well as the fitting R^2 coefficients of the power law relationship for each region are given in Table 3. The higher value of the n exponent found under compressive loadings highlights the distortional hardening behavior. The different values in the orthogonal directions evidence the presence of anisotropic strain hardening in the Ti-6Al-4V alloy.

Table 2. Summary of the mechanical properties directly determined from the true stress–true strain curve presented in Figure 4a.

Testing Loading	Orthogonal Material Direction	Strain, Rate, $\dot{\varepsilon}$ S^{-1}	Young's Modulus, E (GPa)	Initial Yield Strength, $\sigma_{0.2\%}$ (MPa)	Ultimate Tensile Strength, UTS (MPa)	Uniform Elongation, ε_u	Global Hardening Exponent, n	True Fracture Strain, ε_f	True Stress at Fracture MPa
Tension	LD	0.001	111 ± 1	927 ± 3	951	0.10	0.045	0.41	1241
	TD	0.001	115 ± 4	933 ± 1	982	0.97	0.043	0.40	1349
Compression	LD	0.001	122 ± 1	968 ± 3	-	-	0.052	-	-
	TD	0.001	128 ± 3	1040 ± 6	-	-	0.059	-	-

Note: Due to the experimental set-up, the UTS, ε_u, ε_f and true stress at fracture were not possible to acquire for the compression tests.
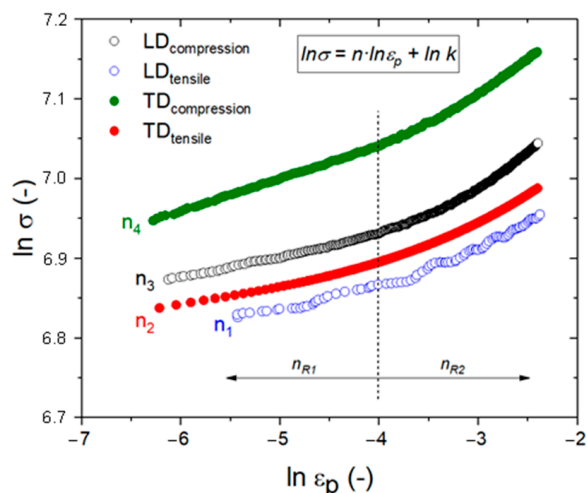
Figure 5. Log-log representation of true stress (ln σ) and true plastic strain (ln ε_p). Range of interest: $0\% \leq \varepsilon_p \leq 9\%$.

Table 3. Summary of the strain-hardening exponents of the power law relationship determined in both regions with their respective fitting coefficients R^2. n_{R1} and n_{R2} denote the n exponent for each region present in Figure 5.

Loading Stress	Material Direction	n_{R1} (−)	n_{R2} (−)	R^2_{R1} (−)	R^2_{R2} (−)
T	LD	$2.77 \times 10^{-2} \pm 9.45 \times 10^{-4}$	$5.86 \times 10^{-2} \pm 9.03 \times 10^{-4}$	0.966	0.987
	TD	$2.81 \times 10^{-2} \pm 4.68 \times 10^{-4}$	$6.13 \times 10^{-2} \pm 3.96 \times 10^{-4}$	0.986	0.993
C	LD	$2.95 \times 10^{-2} \pm 2.48 \times 10^{-4}$	$7.71 \times 10^{-2} \pm 4.36 \times 10^{-4}$	0.995	0.987
	TD	$4.16 \times 10^{-2} \pm 1.08 \times 10^{-4}$	$7.99 \times 10^{-2} \pm 2.49 \times 10^{-4}$	0.999	0.994

3.3. Micro- and Nanomechanical Properties

3.3.1. Loading/Unloading Curve

Typical loading–displacement (P–h) curves generated with the Berkovich indenter into the surface for monotonic loading performed under the displacement control mode are shown in Figure 6 for the LD and TD directions. The P–h curve for the LD direction exhibits the lowest applied load under maximum displacement into the surface after the indenter is withdrawn, confirming that this direction is softer than TD and pointing out the strong anisotropy effect of the Ti-6Al-4V alloy. No discontinuities during the loading curve could be detected for the LD and TD directions.
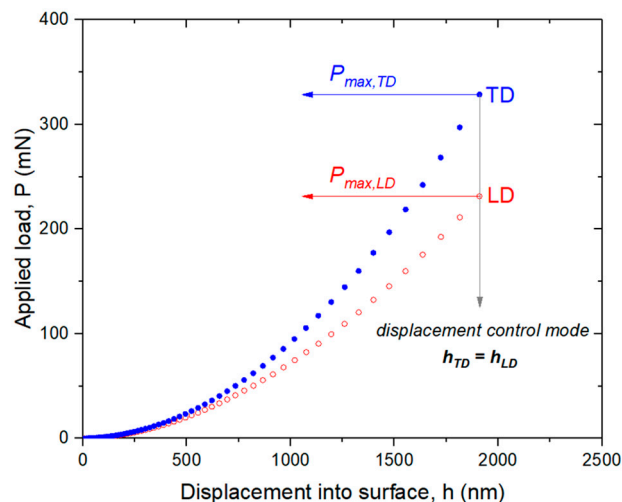

Figure 6. Loading curves for both the orthogonal directions investigated here (LD and TD).

3.3.2. Mechanical Properties of the Ti-6Al-4V Alloy from Nanoindentation

A continuous computation of hardness and elastic modulus as a function of the maximum displacement into the surface of the polycrystalline alloy are shown in Figure 7. As appreciated, the behavior of the indented material is affected by the penetration depth. For indents shallower than 200 nm, hardness and elastic modulus values are strongly affected by length scale or indentation size effects. However, these values tend to stabilize, within the experimental error range, as the penetration depth increases beyond 200 nm.
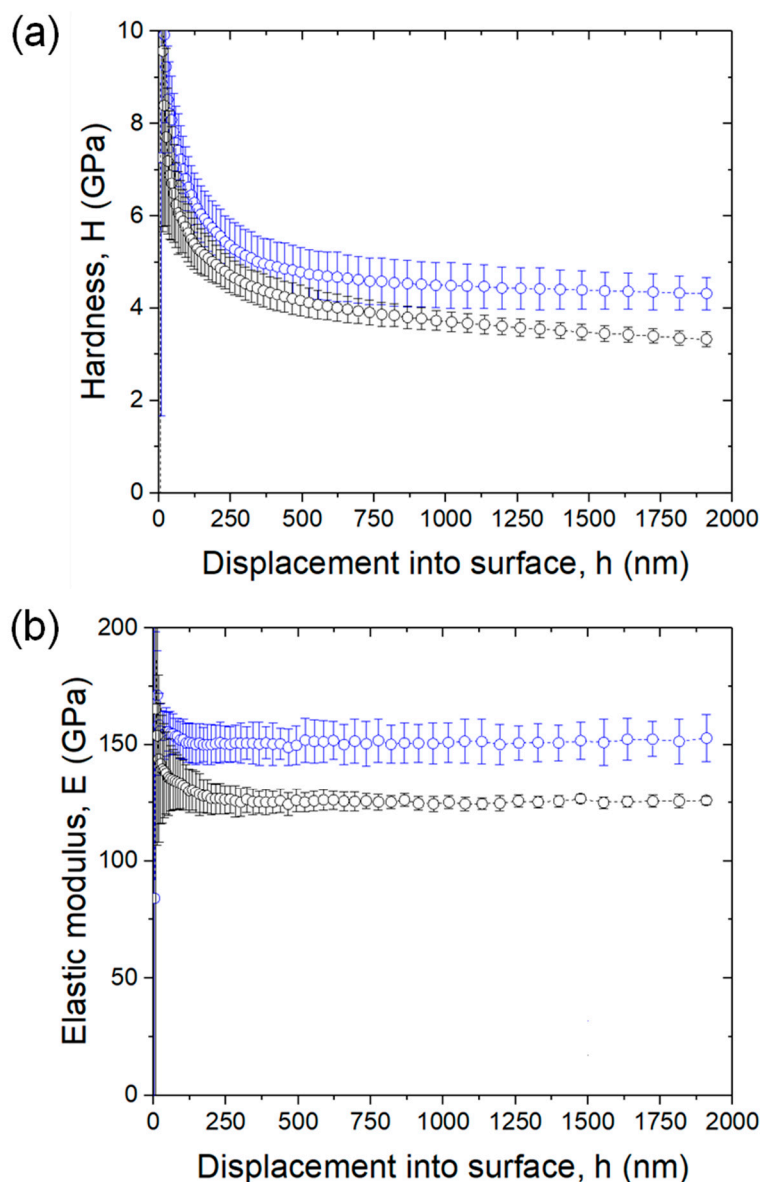

Figure 7. Micromechanical properties: (**a**) hardness and (**b**) elastic modulus vs. displacement into the surface; a function of the loading direction (LD and TD in black and blue, respectively).

Hardness and elastic modulus values obtained as an average in the stabilized zone at the micrometric length scale for the LD and TD are summarized in Table 4. The Ti-6Al-4V alloy found to be strongly anisotropic due to the α-phase at room temperature is strongly anisotropic at the single crystal level, as reported by [46], which depends on the material direction, in terms of hardness and elastic modulus, with the TD orientation being harder and stiffer than the LD. This trend may be associated with the interacting deformation mechanisms. The reported hardness for both orthogonal directions is in fair agreement with the indentation hardness determined through the finite-element approach [47]. Fur-

thermore, the reported hardness obtained by the nanoindentation method is in accordance with previous references, where Han et al. [48] reported a hardness value of the Ti-6Al-4V alloy ranging between 4.09 and 4.71 GPa, and Li et al. [49] found a relative hardness value of around 4.1–5.0 Gpa. Cai et al. [50] reported a hardness value at the micrometric length scale by means of microindentation, which varied from 4.0 to 5.5 Gpa depending on the indentation depth. Babu and coworkers [51] investigated micromechanical properties as a function of the strain rate and found a hardness value ranging between 4.26 and 4.40 GPa for strain rates of 0.05 and 0.20 s^{-1}.

Table 4. Summary of the mechanical properties (hardness, elastic modulus and flow stress) determined using the nanoindentation technique and obtained as an average from the stabilized zone for the commercial Ti-6Al-4V alloy as a function of the material direction.

Material Direction	H (GPa)	E (GPa)	$\sigma_{f\ \text{flow}}$ (GPa)
LD	3.6 ± 0.2	125 ± 2	1.3 ± 0.1
TD	4.5 ± 0.5	151 ± 9	1.7 ± 0.2

The values of the elastic modulus are slightly greater than those determined at the macroscopic length scale (Table 1). This discrepancy could be mainly attributed to the fact that Oliver and Pharr's method based on Sneddon's analysis of elastic contact, as employed here, considers that the effective elastic modulus (E_{eff}) is only affected by the material elastic moduli in the indentation direction and, therefore, does not take into account any of the lateral stresses generated during the indentation process. This stress process produces an overestimation of the elastic modulus through the β parameter, presented in the following equation [10,52]:

$$E_{eff} = \frac{1}{\beta} \frac{\sqrt{\pi}}{2} \frac{S}{\sqrt{A(h_c)}} \tag{1}$$

where β is equal to 1.034 for a Berkovich indenter [53], S is the contact stiffness and $A(hc)$ is the contact area.

It is necessary to highlight that this overestimation does not affect the discussion of the results because all values are equally overestimated. Wen et al. [21], using a spherical indenter at the micrometric length scale, also reported an elastic modulus around 38% higher than the original elastic modulus tested by the conventional stress–strain method. This trend is in fair agreement with the obtained results in both orthogonal directions, summarized in Table 4. Furthermore, the data obtained in this manuscript are around 4 and 25% higher for the LD and TD directions, respectively, than those reported at 2000 nm of maximum displacement into the surface by Babu et al. [47].

One of the key parameters to take into consideration for conducting finite-element modeling (FEM) is the flow stress (σ_{flow}), a critical parameter for reliable evaluation of the energy expended in the flow and fracture. In this sense, this parameter was calculated through the simple convention of previously estimated hardness data. Accordingly, σ_{flow} was reported as the ratio between the measured Vickers hardness (HV) and a constraint factor (ψ), commonly taken as three for soft, ductile metals. A correction factor of 0.9 in ψ was applied, related to the consideration of the Berkovich indenter geometry instead of a Vickers geometry, as reported in [54]. The σ_{flow} for both directions is summarized in Table 4, yielding an upper and lower limit of 1.7 ± 0.2 and 1.3 ± 0.1 GPa for the TD and LD directions, respectively. The σ_{flow} determined by combining the indentation hardness and Tabor's equation is in fair agreement with those reported by Babu et al. [39], who reported a value of 1.12 GPa at a constant strain rate of 0.2 s^{-1}. Furthermore, these values are in concordance with those reported by Kumaraswamy et al. [55], determined under compressive flow stress at average strains ranging between 4% and 7%.

3.3.3. Anisotropy Effect

Once the anisotropy effect was demonstrated, a detailed analysis was performed by making residual imprints at 700 nm of maximum displacement into the surface in order to confine the stress field mainly inside the α-grains. Figure 8 presents typical indentation loading–unloading curves for single indentations performed randomly under a loading control mode of 50 mN. A broad dispersion of P–h curves could be distinguished for both orthogonal directions investigated here (LD and TD directions depicted in Figure 8a,b, respectively). The curves with smaller depth values correspond to indentations made in the α-phase region, whereas the set of curves with higher depths are attributed to indentations made at the α-/β-phases, as represented in Figure 9 (an example is denoted in this figure with a white dashed circle).
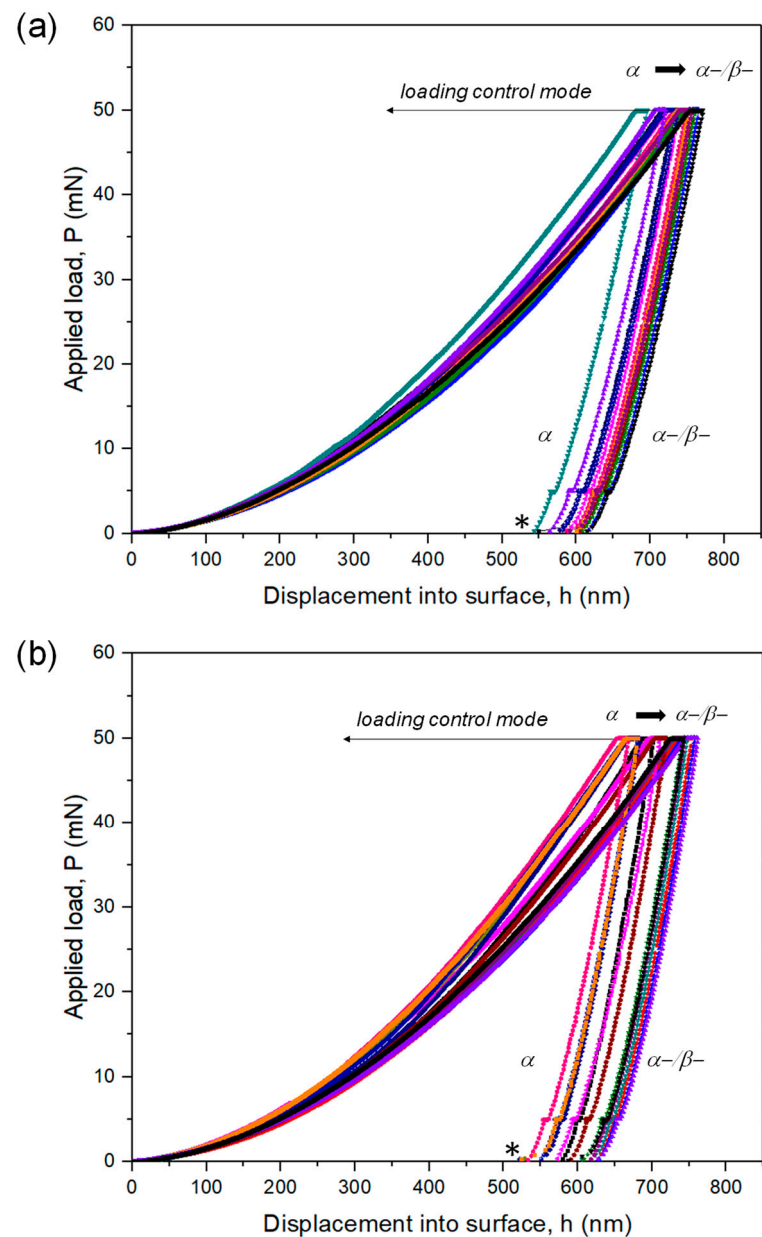

Figure 8. Indentation loading–unloading curves (or P–h curves) performed at 50 mN of maximum applied load for the (**a**) LD and (**b**) TD directions of the Ti-6Al-4V alloys.
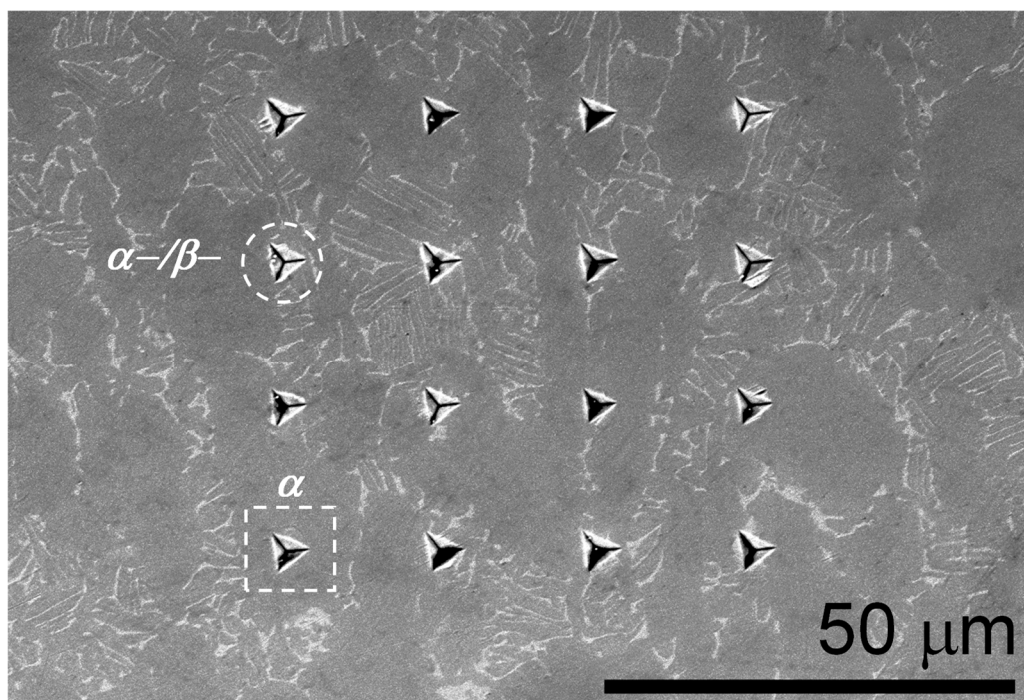
Figure 9. SEM micrograph of one array of imprints performed under the displacement control mode at 700 nm of maximum penetration depth. The white dashed circle denotes an example of a residual imprint performed at the α-/β-interphase.

Furthermore, from the qualitative observation of the P–h curves depicted in Figure 8, it is possible to discern that the α-phase is harder than the zones with α-/β-lamellas. This finding highlights that the β-phase is softer than the α-phase. A similar observation has been reported in the literature [42,56]. Moreover, as can be seen in the unloading curves of Figure 8, from the final penetration depth (see * in Figure 8), the α-phase for the TD is slightly harder than for the LD direction. The results extracted from these curves confirmed the anisotropic behavior as a function of hardness of the Ti-6Al-4V alloy in both directions, with the obtained results for the α-phase being in fair agreement with those summarized in Table 4.

Figure 10 shows the elastic modulus histograms with a 2 GPa bin size, determined from 64 indents per each orthogonal direction. A monomodal peak centered at 109 and 119 GPa for the LD and TD directions, respectively, could be observed. The graphs clearly show that the TD direction is stiffer than the LD direction, with this trend and these elastic modulus values being in good agreement with those obtained by conventional tensile tests in the Ti-6Al-4V alloy, summarized in Table 2 [7]. They are also in concordance with those reported by Kherrouba et al. [57]. The elastic modulus values reported in Figure 10 are between 15% and 26% lower, for the LD and TD orthogonal directions, respectively, than those obtained at maximum displacement into the surface of around 2000 nm (see Table 4 and Figure 7a). This difference may be associated with the fact that data presented in Figure 10 come from tests mainly performed in the α-phase and some of them at the interface between the α-/β-phase. This observation points out that both phases are anisotropic in terms of hardness. As shown in Figure 9, when the residual imprint as well as the plastic flow induced during the indentation process interact with the β-phase, the P–h curve moves to higher displacement into the surfaces (see Figure 8), highlighting that the mechanical behavior of the α-/β-interphase is softer than the mechanical behavior for the α-phase. A similar trend has been observed for the elastic modulus, where the α-phase is stiffer, which is determined by the modulus of the individual phases and their volume fractions as reported by Hao et al. [58], and more sensitive to phase/crystal structure than other factors [59].
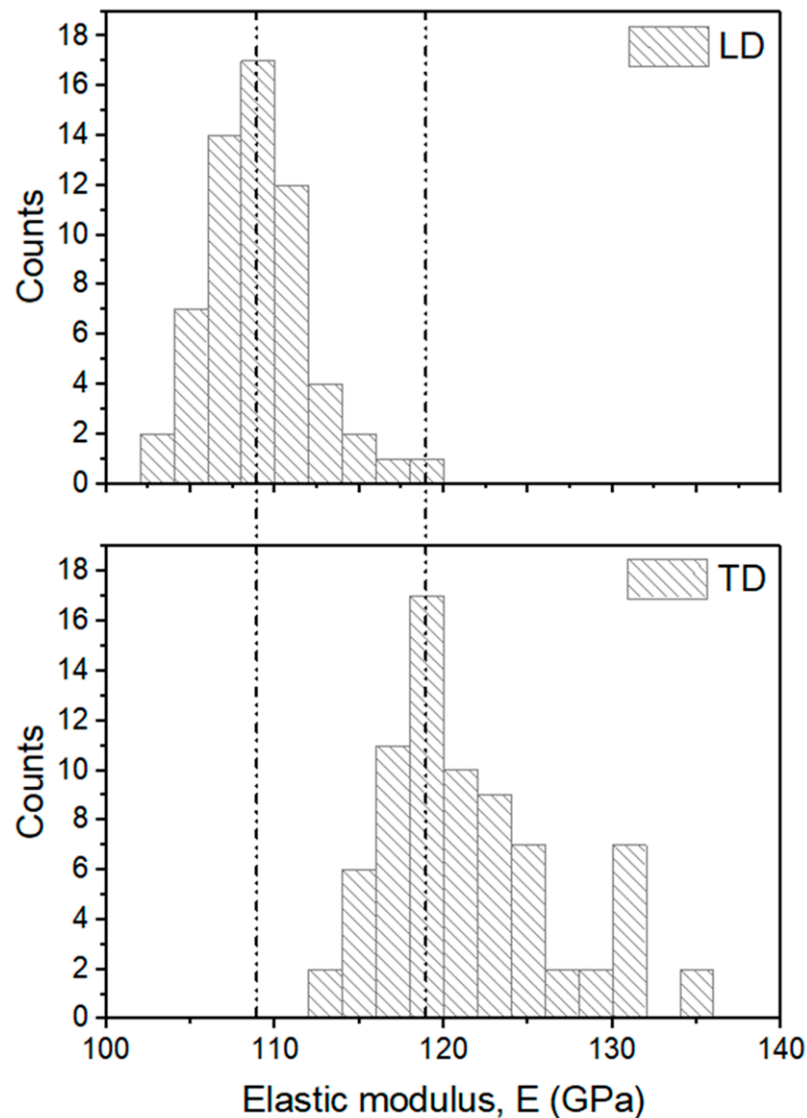
Figure 10. Elastic modulus histograms determined from 64 indents performed at constant displacement into the surface of 700 nm for both orthogonal directions (LD and TD).

3.3.4. Deformation Mechanisms Induced by Nanoindentation

Figure 11 shows a FESEM image corresponding to a homogeneous array of imprints performed at a penetration depth of 2000 nm. Among the numerous possible deformation processes encountered in hexagonal, closely packed metals, slip is the main deformation system of the α-phase at room temperature, as appreciated around the indents shown in Figure 11a. It is clear that the plastic deformation field generated during nanoindentation is confined under the imprint interacting with several grains. A close inspection of some residual imprints is shown in Figure 11b,c, and no plastic deformation induced can be observed. This can be due to the fact that the particular crystallographic orientation is not favorable to activate slip traces and also to the high amount of β-phase, as observed in Figure 3, in the indented zone, which blocks the activation and emergence of the slip traces until reaching the surface. The location of these imprints in a region with a high amount of β-phase implies that higher stress is required to induce slip traces as well as twining. On the other hand, in Figure 11d, the plastic field induced by nanoindentations may be observed around the residual imprint. Furthermore, two transformation twins at the edge of the residual imprint (marked with a white arrow in Figure 11d) with a lenticular shape can be seen. Unlike slip, twinning depends not just on the resolved shear stress but also on its sign. In polycrystalline materials, deformation behavior is mainly governed by the

relative activation of the different deformation mechanisms and their interactions, which strongly depend on the crystallographic texture and deformation mode and, therefore, are difficult to predict.
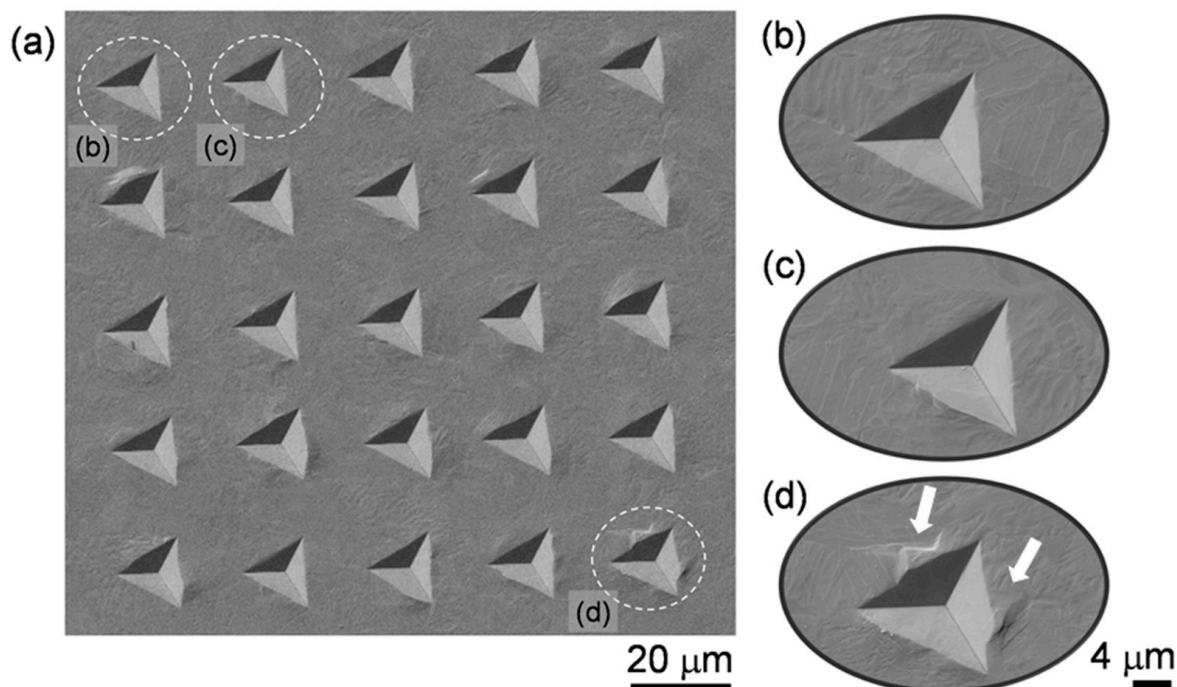

Figure 11. FESEM micrographs showing the residual imprints. (**a**) General view of the array of the residual imprints; (**b–d**) FESEM magnifications of some residual imprints in order to show the different deformation features.

Figure 12 shows a view of a residual imprint entirely embedded within the α-phase. This will also apply for plastic field dimensions, estimated to range between 4.9 and 7.0 μm (i.e., between 7 and 10 times the maximum displacement into the surface), slightly smaller than the mean grain size experimentally determined for the Ti-6Al-4V α-phase. This fact indicates that data gathered from indentations 700 nm in depth are valid for extracting intrinsic hardness values of this phase. Furthermore, no slip traces were observed around the residual imprint, which implies that the crystallographic orientation of the α-phase is not favorable to activate the slip system. Some of the residual imprints are located near the center of α-grains, whereas others are located nearer to the grain boundaries or even in the β-phase. In the present study, only nanoindents near the center of α-grains were taken into consideration in order to minimize the influence of grain boundaries and the β-phase on extracted values of the constitutive hardness. Thus, a hardness value for the α-phase between 5.3 and 7.1 GPa was obtained. This significant trend may be associated with the specific crystallographic orientation for the α-grains, and the highest hardness value may be associated with an α-grain with a crystallographic orientation near the [0001] stress axis, the latter in fair agreement with the values reported by Viswanathan et al. [60]. In addition, the hardness value decreases as the indentation stress axis induced during the indentation process deviates from the [0001] orientation [47].

The relationship between flow stress obtained at the macroscopic length scale under different stress fields (tensile and compression) and the flow stress determined at the micrometric length scale can be graphically displayed using Tabor's equation. At the macroscopic length scale, Figure 13a represents the flow stress determined through the compression (*y*-axis) and tensile tests (*x*-axis). Figure 13b displays the linear relationship between the compressive flow stress and the flow stress determined using the composite hardness (hardness taking into account both constitutive phases in the Ti-6Al-4V alloys, α-/β-) combined with Tabor's equation.
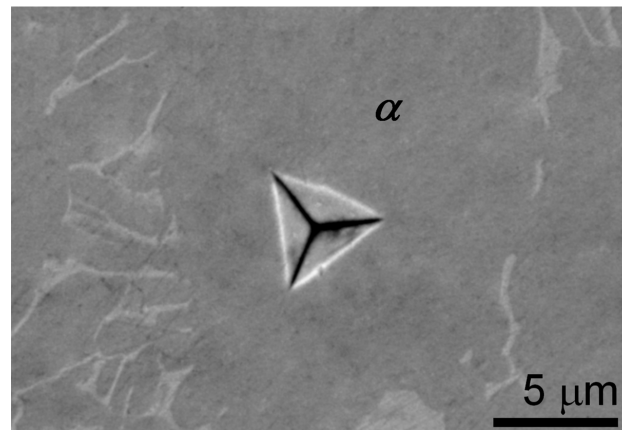
Figure 12. FESEM magnification micrograph of a specific location of a residual imprint performed at 700 nm of maximum displacement into the surface, where individual imprints within the Ti-6Al-4V α-phase are clearly appreciated (white dashed square presented in Figure 9).

3.4. Mechanical Properties Correlation: From the Macro- to Nanometric Length Scale

Furthermore, under the current investigated conditions (in terms of loads, stresses, strains, room temperature and quasistatic state), the flow stress determined at the macroscopic length scale under different stress fields (compression and/or tensile) can be predicted with a simple nanoindentation test and subsequently using Tabor's expression. In other words, if all the testing parameters are controlled, a simple predictive model can be obtained in which a nanoindentation test can be used to estimate both the flow stress under compression (equation provided in Figure 13b) and tensile stresses using the following expression:

$$\sigma_{flow,tensile} = 0.908 + 0.015 \cdot \sigma_{flow,nanoindentation} \tag{2}$$

Taking into account Tabor's equation, $\sigma_{flow} = H_{composite}/(3 \cdot \psi)$, where $H_{composite}$ refers to the bulk material properties, Equation (2) can be rewritten in terms of the composite nanoindentation hardness as follows:

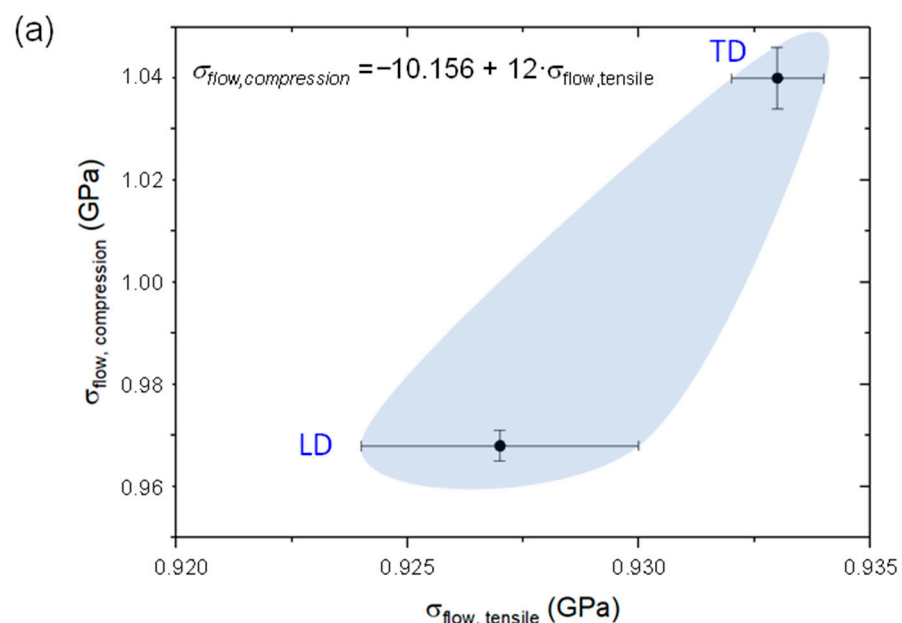$$\sigma_{flow,tensile} = 0.908 + 5.56 \times 10^{-3} \cdot H_{composite} \tag{3}$$
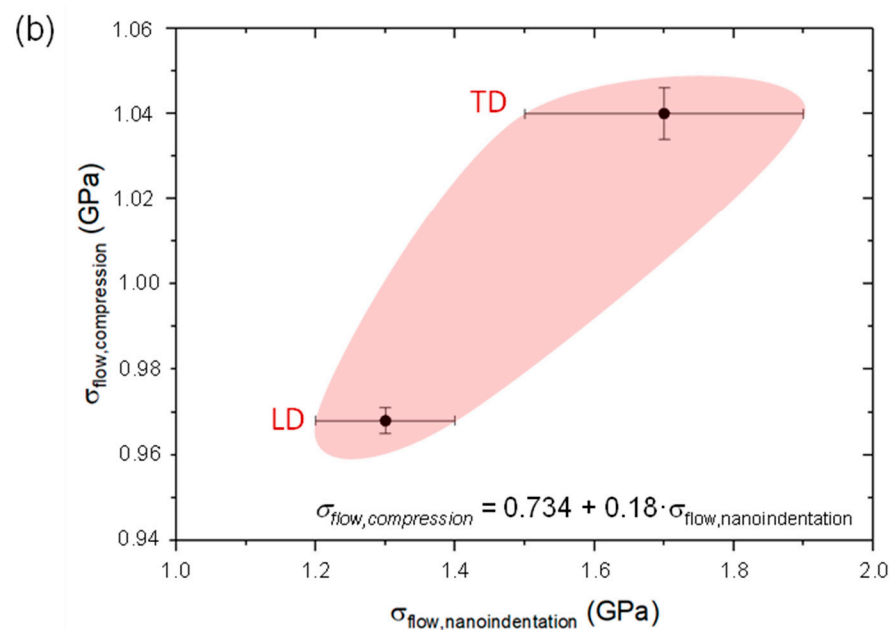

Figure 13. *Cont.*

Figure 13. Relationship between flow stress determined under different stress fields and also at different length scales. (**a**) Flow stress under compression vs. under the tensile test; both tests were performed at the macroscopic length scale and (**b**) flow stress under compression (macroscopic length scale) vs. the one determined at the micrometric length scale using the composite indentation hardness and Tabor's equation.

This predictive model has a potential practical implication since by only measuring a single mechanical property, the flow stress under different deformation fields can be obtained at the macroscopic length scale, thus avoiding the machining of both tension and compression specimens (see Figure 2), of which the procedure is expensive, time and material consuming and cumbersome to perform in the industry.

4. Conclusions

Based on the obtained results for the investigated Ti-6Al-4V alloy, the following conclusions can be drawn:

(1) The mechanical properties tested under different stress fields at the macroscopic length scale present different mechanical behavior, with compression being slightly higher than that obtained by tensile tests.

(2) The stress–strain curves at the macroscopic length scale are strongly anisotropic depending on the testing direction, with flow stress and hardening being around 20–25% higher for the TD direction than for the LD direction.

(3) The hardness, elastic modulus and flow stress values at the submicrometric length scale for the TD direction are around 25, 21 and 32% higher than those measured for the LD direction.

(4) The P–h curves for the α- and α-/β-interphase indicate that the α-phase is harder, highlighting that the β-phase may be softer than the other two constituents in the Ti-6Al-4V alloy.

(5) The high amount of β-phase heterogeneously distributed in the α-phase is responsible for blocking the activation and the emergence of the slip traces until reaching the surface.

(6) A simple mathematical relationship can be obtained relating the flow stress determined under different stress fields as well as at different length scales, highlighting that the values reported under tensile, compression and even nanoindentation tests are governed by the pre-existing microstructure.

References

1. Bettaieb, M.B.; Van Hoof, T.; Minnebo, H.; Pardoen, T.; Dufour, P.; Jacques, P.; Habraken, A.M. Micromechanics-Based Damage Analysis of Fracture in Ti5553 Alloy with Application to Bolted Sectors. *J. Mater. Eng. Perform.* **2015**, *24*, 1262–1278. [CrossRef]
2. Tuninetti, V.; Habraken, A.M. Impact of anisotropy and viscosity to model the mechanical behavior of Ti–6Al–4V alloy. *Mater. Sci. Eng. A* **2014**, *605*, 39–50. [CrossRef]
3. Lütjering, G.; Williams, J.C. *Titanium (Engineering Materials and Processes)*; Springer: Berlin/Heidelberg, Germany, 2003; ISBN 978-3-662-13222-7.
4. Peters, M.; Kumpfert, J.; Ward, C.; Leyens, C. Titanium Alloys for Aerospace Applications. *Adv. Eng. Mater.* **2003**, *5*, 419–427. [CrossRef]
5. Wei, D.; Koizumi, Y.; Chiba, A. Discontinuous yielding and microstructural evolution of Ti-40 at.% Al alloy compressed in single α-hcp phase region. *J. Alloys Compd.* **2017**, *693*, 1261–1276. [CrossRef]
6. Wang, Q.; Shankar, M.R.; Liu, Z. Visco-plastic self-consistent modeling of crystallographic texture evolution related to slip systems activated during machining Ti-6AL-4V. *J. Alloys Compd.* **2021**, *853*, 157336. [CrossRef]
7. Hémery, S.; Tromas, C.; Villechaise, P. Slip-stimulated grain boundary sliding in Ti-6Al-4 V at room temperature. *Materialia* **2019**, *5*, 100189. [CrossRef]
8. Htwe, Y.; Kwak, K.; Kishi, D.; Mine, Y.; Ding, R.; Bowen, P.; Takashima, K. Anisotropy of <a> slip behaviour in single-colony lamellar structures of Ti–6Al–4V. *Mater. Sci. Eng. A* **2018**, *715*, 315–319. [CrossRef]
9. Jun, T.-S.; Sernicola, G.; Dunne, F.P.; Britton, T.B. Local deformation mechanisms of two-phase Ti alloy. *Mater. Sci. Eng. A* **2016**, *649*, 39–47. [CrossRef]
10. Hosford, W.F.; Caddell, R.M. *Metal Forming: Mechanics and Metallurgy*, 3rd ed.; Cambridge University Press: Cambridge, UK, 2011.
11. Hutchinson, B. Critical Assessment 16: Anisotropy in metals. *Mater. Sci. Technol.* **2015**, *31*, 1393–1401. [CrossRef]
12. Tuninetti, V.; Gilles, G.; Milis, O.; Pardoen, T.; Habraken, A.-M. Anisotropy and tension–compression asymmetry modeling of the room temperature plastic response of Ti–6Al–4V. *Int. J. Plast.* **2015**, *67*, 53–68. [CrossRef]
13. Gilles, G.; Hammami, W.; Libertiaux, V.; Cazacu, O.; Yoon, J.; Kuwabara, T.; Habraken, A.; Duchêne, L. Experimental characterization and elasto-plastic modeling of the quasi-static mechanical response of TA-6V at room temperature. *Int. J. Solids Struct.* **2011**, *48*, 1277–1289. [CrossRef]
14. Chen, L.; Zhang, H.; Song, M. Extension of Barlat's Yield Criterion to Tension–Compression Asymmetry: Modeling and Verification. *Metals* **2020**, *10*, 713. [CrossRef]
15. Amna, Z.; Olfa, D.; Gahbiche, A.; Nasri, R. Identification strategy of anisotropic behavior laws: Application to thin sheets of Aluminium A5. *J. Theor. Appl. Mech.* **2016**, *54*, 1147–1156. [CrossRef]
16. Olfa, D.; Amna, Z.; Amen, G.; Rachid, N. Identification of the anisotropic behavior of an aluminum alloy subjected to simple and cyclic shear tests. *Proc. Inst. Mech. Eng. Part C J. Mech. Eng. Sci.* **2018**, *233*, 911–927. [CrossRef]
17. Tuninetti, V.; Gilles, G.; Flores, P.; Pincheira, G.; Duchêne, L.; Habraken, A.-M. Impact of distortional hardening and the strength differential effect on the prediction of large deformation behavior of the Ti6Al4V alloy. *Meccanica* **2019**, *54*, 1823–1840. [CrossRef]
18. Roa, J.; Suarez, S.; Guitar, A.; Fargas, G.; Mateo, A.M. Geometrically Necessary Dislocations on Plastic Deformation of Polycrystalline TRIP Steel. *Crystals* **2019**, *9*, 289. [CrossRef]
19. Roa, J.; Suarez, S.; Yang, H.; Fargas, G.; Guitar, A.; Rayón, E.; Green, I.; Mateo, A. Influence of the Crystallographic Orientation on the Yield Strength and Deformation Mechanisms of Austenitic Grains in Metastable Stainless Steels Investigated by Spherical Nanoindentation. *Steel Res. Int.* **2019**, *90*, 1800425. [CrossRef]
20. Roa, J.; Fargas, G.; Mateo, A.; Piqué, E.J. Dependence of nanoindentation hardness with crystallographic orientation of austenite grains in metastable stainless steels. *Mater. Sci. Eng. A* **2015**, *645*, 188–195. [CrossRef]
21. Wen, Y.; Xie, L.; Wang, Z.; Wang, L.; Lu, W.; Zhang, L.-C. Nanoindentation characterization on local plastic response of Ti-6Al-4V under high-load spherical indentation. *J. Mater. Res. Technol.* **2019**, *8*, 3434–3442. [CrossRef]

22. Majumdar, P.; Singh, S.; Chakraborty, M. Elastic modulus of biomedical titanium alloys by nano-indentation and ultrasonic techniques—A comparative study. *Mater. Sci. Eng. A* **2008**, *489*, 419–425. [CrossRef]
23. Jun, T.-S.; Armstrong, D.E.; Britton, T.B. A nanoindentation investigation of local strain rate sensitivity in dual-phase Ti alloys. *J. Alloys Compd.* **2016**, *672*, 282–291. [CrossRef]
24. Uchic, M.D.; Dimiduk, D.M. A methodology to investigate size scale effects in crystalline plasticity using uniaxial compression testing. *Mater. Sci. Eng. A* **2005**, *400*, 268–278. [CrossRef]
25. Broitman, E. Indentation Hardness Measurements at Macro-, Micro-, and Nanoscale: A Critical Overview. *Tribol. Lett.* **2017**, *65*, 23. [CrossRef]
26. Tuninetti, V.; Gilles, G.; Milis, O.; Lecarme, L.; Habraken, A.M. Compression test for plastic anisotropy characterization using optical full-field displacement measurement technique. *Steel Res. Int.* **2012**, 1239–1242.
27. Tuninetti, V.; Flores, P.; Valenzuela, M.; Pincheira, G.; Medina, C.; Duchêne, L.; Habraken, A.-M. Experimental characterization of the compressive mechanical behaviour of Ti6Al4V alloy at constant strain rates over the full elastoplastic range. *Int. J. Mater. Form.* **2020**, *13*, 709–724. [CrossRef]
28. Tuninetti, V.; Gilles, G.; Péron-Lührs, V.; Habraken, A.M. Compression Test for Metal Characterization using Digital Image Correlation and Inverse Modeling. *Procedia IUTAM* **2012**, *4*, 206–214. [CrossRef]
29. Oliver, W.; Pharr, G. An improved technique for determining hardness and elastic modulus using load and displacement sensing indentation experiments. *J. Mater. Res.* **1992**, *7*, 1564–1583. [CrossRef]
30. Oliver, W.; Pharr, G. Measurement of hardness and elastic modulus by instrumented indentation: Advances in understanding and refinements to methodology. *J. Mater. Res.* **2004**, *19*, 3–20. [CrossRef]
31. Nixon, M.E.; Cazacu, O.; Lebensohn, R.A. Anisotropic response of high-purity α-titanium: Experimental characterization and constitutive modeling. *Int. J. Plast.* **2010**, *26*, 516–532. [CrossRef]
32. Salem, A.A.; Kalidindi, S.R.; Doherty, R.D. Strain hardening of titanium: Role of deformation twinning. *Acta Mater.* **2003**, *51*, 4225–4237. [CrossRef]
33. Hama, T.; Nagao, H.; Kobuki, A.; Fujimoto, H.; Takuda, H. Work-hardening and twinning behaviors in a commercially pure titanium sheet under various loading paths. *Mater. Sci. Eng. A* **2015**, *620*, 390–398. [CrossRef]
34. Hirth, J.P.; Lothe, J. *Theory of Dislocations*, 2nd ed.; McGraw-Hill: New York, NY, USA, 1968.
35. Kocks, U.F. A statistical theory of flow stress and work-hardening. *Philos. Mag.* **1966**, *13*, 541–566. [CrossRef]
36. Kuhlmann, W.D. Theory of Plastic Deformation: -Properties of low energy dislocation structures. *Mater. Sci. Eng. A* **1989**, *A113*, 1–41. [CrossRef]
37. Ludwik, P. Einfluβ der Deformationsfeschwindigkeit Mit Besonderer Berücksichtigung der Nackwirkungsercheinungen. In *Elemente der Technologischen Mechanik*; Springer: Berlin, Germany, 1909; pp. 44–53.
38. Swift, H. Plastic instability under plane stress. *J. Mech. Phys. Solids* **2002**, *1*, 1–18. [CrossRef]
39. Voce, E. The relationship between stress and strain for homogeneous deformation. *J. Inst. Metal.* **1984**, *74*, 537–562.
40. Kocks, U.; Mecking, H. Physics and phenomenology of strain hardening: The FCC case. *Prog. Mater. Sci.* **2003**, *48*, 171–273. [CrossRef]
41. Taylor, G. Plastic strain in metals. *J. Inst. Met.* **1938**, *62*, 307–324.
42. Estrin, Y.; Tóth, L.; Molinari, A.; Bréchet, Y. A dislocation-based model for all hardening stages in large strain deformation. *Acta Mater.* **1998**, *46*, 5509–5522. [CrossRef]
43. Arsenlis, A.; Parks, D. Crystallographic aspects of geometrically-necessary and statistically-stored dislocation density. *Acta Mater.* **1999**, *47*, 1597–1611. [CrossRef]
44. Austin, R.A.; McDowell, D.L. A dislocation-based constitutive model for viscoplastic deformation of fcc metals at very high strain rates. *Int. J. Plast.* **2011**, *27*, 1–24. [CrossRef]
45. Matusevich, A.E.; Massa, J.C.; Mancini, R.A. Computation of Tensile Strain-Hardening Exponents through the Power-Law Relationship. *J. Test. Eval.* **2012**, *40*, 104226. [CrossRef]
46. Partridge, P.G. The crystallography and deformation modes of hexagonal close-packed metals. *Met. Rev.* **1967**, *12*, 169–194. [CrossRef]
47. Babu, B.S.; Srikanth, V.; Balram, Y.; Vishnuvardhan, T.; Baig, M.A.A. Numerical analysis on the indentation behavior of Ti-6Al-4V alloy. *Mater. Today Proc.* **2019**, *19*, 827–830. [CrossRef]
48. Han, F.; Tang, B.; Kou, H.; Li, J.; Feng, Y. Experiments and crystal plasticity finite element simulations of nanoindentation on Ti–6Al–4V alloy. *Mater. Sci. Eng. A* **2015**, *625*, 28–35. [CrossRef]
49. Li, R.; Riester, L.; Watkins, T.; Blau, P.J.; Shih, A.J. Metallurgical analysis and nanoindentation characterization of Ti–6Al–4V workpiece and chips in high-throughput drilling. *Mater. Sci. Eng. A* **2008**, *472*, 115–124. [CrossRef]
50. Cai, J.; Li, F.; Liu, T.; Chen, B. Investigation of mechanical behavior of quenched Ti–6Al–4V alloy by microindentation. *Mater. Charact.* **2011**, *62*, 287–293. [CrossRef]
51. Sridharbabu, B.; Kumaraswamy, A.; AnjaneyaPrasad, B. Effect of Indentation Size and Strain Rate on Nanomechanical Behavior of Ti-6Al-4VAlloy. *Trans. Indian Inst. Met.* **2014**, *68*, 143–150. [CrossRef]
52. Hay, J.C.; Bolshakov, A.; Pharr, G.M. A critical examination of the fundamental relations used in the analysis of nanoindentation data. *J. Mater. Res.* **1999**, *14*, 2296–2305. [CrossRef]
53. King, R. Elastic analysis of some punch problems for a layered medium. *Int. J. Solids Struct.* **1987**, *23*, 1657–1664. [CrossRef]

54. Casals, O.; Alcalá, J. The duality in mechanical property extractions from Vickers and Berkovich instrumented indentation experiments. *Acta Mater.* **2005**, *53*, 3545–3561. [CrossRef]
55. Kumaraswamy, A.; Rao, V.V. High strain-rate plastic flow behavior of Ti–6Al–4V from dynamic indentation experiments. *Mater. Sci. Eng. A* **2011**, *528*, 1238–1241. [CrossRef]
56. Dong, J.; Li, F.; Wang, C. Micromechanical behavior study of α phase with different morphologies of Ti–6Al–4V alloy by microindentation. *Mater. Sci. Eng. A* **2013**, *580*, 105–113. [CrossRef]
57. Kherrouba, N.; Carron, D.; Bouabdallah, M.; Badji, R. Effect of Solution Treatment on the Microstructure, Micromechanical Properties, and Kinetic Parameters of the β → α Phase Transformation during Continuous Cooling of Ti-6Al-4V Titanium Alloy. *J. Mater. Eng. Perform.* **2019**, *28*, 6921–6930. [CrossRef]
58. Hao, Y.L.; Yang, R.; Niinomi, M.; Kuroda, D.; Zhou, Y.L.; Fukunaga, K.; Suzuki, A. Young's modulus and mechanical properties of Ti-29Nb-13Ta-4.6Zr in relation to α″ martensite. *Met. Mater. Trans. A* **2002**, *33*, 3137–3144. [CrossRef]
59. Ho, W.; Ju, C.; Lin, J.C. Structure and properties of cast binary Ti–Mo alloys. *Biomaterials* **1999**, *20*, 2115–2122. [CrossRef]
60. Viswanathan, G.; Lee, E.; Maher, D.M.; Banerjee, S.; Fraser, H.L. Direct observations and analyses of dislocation substructures in the α phase of an α/β Ti-alloy formed by nanoindentation. *Acta Mater.* **2005**, *53*, 5101–5115. [CrossRef]